Absence of edge states in the valley Chern insulator in moiré graphene

Ahmed Khalifa, Ganpathy Murthy, and Ribhu K. Kaul, and Ribhu K. Kaul ¹Department of Physics & Astronomy, University of Kentucky, Lexington, Kentucky 40506, USA ²Department of Physics, The Pennsylvania State University, University Park, Pennsylvania 16802, USA

(Received 18 September 2022; accepted 6 February 2023; published 22 February 2023)

We study the edge spectrum of twisted sheets of single layer and bilayer graphene in cases where the continuum model predicts a valley Chern insulator—an insulating state in which the occupied moiré mini-bands from each valley have a net Chern number, but both valleys together have no net Chern number, as required by time-reversal symmetry. In a simple picture, such a state might be expected to have chiral valley polarized counterpropagating edge states. We present results from exact diagonalization of the tight-binding model of commensurate structures in the ribbon geometry. We find that for both the single-layer and bilayer moiré ribbons robust edge modes are generically absent. We attribute this lack of edge modes to the fact that the edge induces valley mixing.

DOI: 10.1103/PhysRevB.107.085138

I. INTRODUCTION

Research in moiré materials has exploded in the past few years since the discovery of superconductivity and Mott insulators in twisted bilayer graphene (TBG) [1-3]. Subsequent experimental studies have shown similar physics in graphene multilayers such as twisted double bilayer graphene (TDBG) [4–8] and trilayer graphene on a hexagonal boron nitride substrate [9–11].

At low energies and small twist angles, in the bulk of a moiré system, one makes the continuum approximation [12,13], in which each valley is studied independently and has a moiré band structure. The moiré bands in each valley can have nonzero Chern numbers. However, time-reversal symmetry forces bands arising in opposite valleys, and related by time-reversal, to have opposite Chern numbers. This raises the interesting possibility that when two such bands in opposite valleys are occupied one has a valley Chern insulator. Since the Chern number dictates the chirality of edge modes, the valley Chern insulator could, in principle, realize valleyfiltered counterpropagating edge modes. However, this picture is questionable, since it is likely that absent any new mechanism, an edge would produce strong intervalley scattering. Such intervalley scattering is expected to cause backscattering between the counterpropagating edge modes resulting in the localization of the would-be edge states.

Thus, it is somewhat surprising that a recent experiment on twisted double bilayer graphene near charge neutrality [14] found nonlocal transport in this system, which can be interpreted in terms of robust edge states of the valley Chern insulator phase. This raises the question of whether there might be some hidden mechanism that suppresses intervalley scattering at the edge in a moiré system.

To study this question further, we first study the continuum model and find sets of parameters that result in a valley Chern insulator (Sec. II). Turning to tight-binding models on the lattice, show that in bulk commensurate systems at small angles, a distinction between trivial and valley Chern insulators requires the commensurate structure to have an exact C_3 symmetry (which is achieved by twisting around a carbon site or honeycomb center with AA stacking) in Sec. III. Next, we study generic lattice structures in the ribbon geometry and find that protected edge modes are absent in Sec. IV A. We repeat our calculations for the twisted double bilayer graphene in Sec. IVB and show that no protected edge modes exist here either. We briefly summarize our results and present our conclusions in Sec. V.

II. VALLEY CHERN INSULATORS IN THE CONTINUUM MODEL OF TWISTED BILAYER GRAPHENE

A good starting point for studying moiré physics is the continuum model of twisted bilayer graphene [12,13]. This model, which is well justified for small twist angles for bands near the charge neutral point, is based on the tunneling between the two Dirac cones (in a single valley) of the two graphene layers. In real space, the single valley continuum model reads

$$H_{\text{cont}}(\mathbf{r}) = \begin{pmatrix} -iv_F \boldsymbol{\sigma} \cdot \nabla_{\theta/2} & U(\mathbf{r}) \\ U^{\dagger}(\mathbf{r}) & -iv_F \boldsymbol{\sigma} \cdot \nabla_{-\theta/2} \end{pmatrix}, \quad (1)$$

where $\sigma = (\sigma_x, \sigma_y)$ is a Pauli matrix vector representing the sublattice index of graphene. The diagonal elements of the matrix represent the low-energy continuum Hamiltonian near the Dirac point within each layer. Note that the gradient term is rotated in each layer by $\pm \theta/2$. The graphene Fermi velocity v_F is expressed in terms of the nearest-neighbor hopping strength t, as $v_F = -\sqrt{3}ta/(2\hbar)$, where \hbar is set to 1 and a is the graphene lattice constant which we also set to 1 so that v_F has the units of energy. For the following, we use the numerical value t = -2.7 eV to obtain the band structure

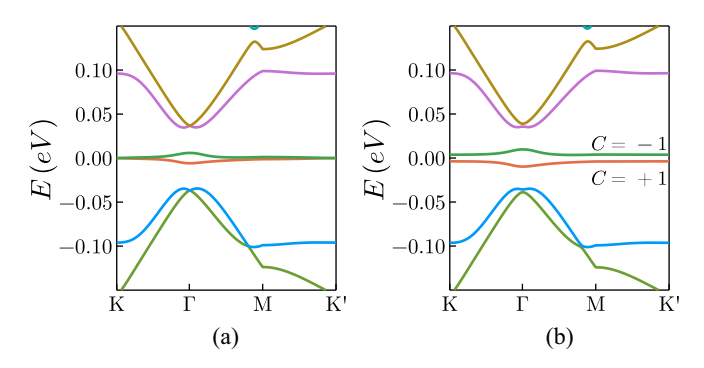


FIG. 1. Single valley band structure of the continuum model at the magic angle ($\alpha=0.6051$ and $\kappa=0.7$). (a) shows the bands before adding sublattice masses to the layers and the Dirac touchings at the K, K' points protected by the $C_2\mathcal{T}$ symmetry. (b) A gap opens up at the K, K' points when sublattice masses are added (We used $m_t=0.01, m_b=0.01eV$). The conduction and the valence bands acquire opposite Chern numbers. By time-reversal symmetry, bands in the other valley have the opposite Chern numbers as their time-reversed partners.

(Fig. 1). The tunneling between the layers is encapsulated in the $U(\mathbf{r})$ term which reads

$$U(\mathbf{r}) = \sum_{j=1}^{3} T_j e^{i\mathbf{q}_j \cdot \mathbf{r}},$$
 (2)

where $T_j = w_0 + w_1 e^{(i2\pi/3)j\sigma_z} \sigma_x e^{(-i2\pi/3)j\sigma_z}$ with w_0 and w_1 denoting the strength of AA and AB hopping, respectively, and $q_1 = (0, -k_\theta)$, $q_2 = C_3 q_1$, $q_3 = C_3 q_2$, where k_θ is the difference between the rotated Dirac points in each layer. Lattice relaxation effects generally make the AB hopping more favorable than AA hopping [15,16]. This is incorporated into the model by making $w_0 < w_1$ with $\kappa = w_0/w_1$ denoting the ratio between the two. Taking the extreme limit $w_0 = 0$ leads to the chiral model of TBG [17]. The rotation of the Dirac Hamiltonian in each layer is usually ignored at small twist angles due to the fact that θ is small (≈ 0.01). When this approximation is made, the continuum model becomes a function of a dimensionless parameter $\alpha = w_1/(v_F k_\theta)$ and the ratio κ . The most studied feature of the continuum model is a pair of nearly flat (exactly flat in the chiral model) bands (per valley per spin) at the magic angles [13,18]. These bands are isolated from high-energy bands by an energy gap.

The single-valley continuum model has several emergent symmetries that constrain its band structure and its topological properties [19–21]. Of particular interest is the $C_2\mathcal{T}$ symmetry which protects a Dirac touching at the K and K' points of the moiré Brillouin zone [BZ; see Fig. 1(a)]. Upon breaking this symmetry a gap opens up at the K, K' points. This symmetry breaking can be achieved experimentally by aligning the graphene layers with the hexagonal boron nitride (HBN) substrate as has been shown before in the single layer [22–28]. The effect of the HBN substrates is modeled by adding a uniform C_2 breaking mass on the top and the bottom layer. Thus, equation (1) becomes

$$H(\mathbf{r}) = H_{\text{cont}}(\mathbf{r}) + \begin{pmatrix} m_t \sigma_z & 0\\ 0 & m_b \sigma_z \end{pmatrix}.$$
 (3)

In addition to opening up a gap at the *K*, *K'* points, the two flat bands can acquire nonzero Chern numbers while the remote bands remain trivial (see Appendix C for a complete discussion). Time-reversal forces the Chern numbers of corresponding bands in opposite valleys to have opposite Chern numbers [see Fig. 1(b)]. Adding the effects of electron-electron interactions to this one-body picture can explain the observation of the quantum anomalous Hall effect in TBG devices that are aligned with HBN [29–31]. In brief, the quantum anomalous Hall effect can be understood as the result of spontaneously breaking time-reversal symmetry when the electrons fill a single-valley flat band with nonzero Chern number [32–38].

As described before, the valley Chern insulator is a time-reversal-symmetric band insulator in which each valley has a nonzero Chern number (but the two valleys have opposite Chern numbers by time reversal). The valley Chern number is defined by integrating the Berry curvature of one valley on the moiré Brillouin zone. In the continuum model, the valley Chern number in the TBG-HBN system is well defined due to the conservation of charge in each valley. We note that, unlike the quantum anomalous Hall phase, this state does not require electron-electron interactions. The continuum model of the TBG-HBN structure suggests that the system can realize a valley Chern insulator phase at charge neutrality in which the two valleys have opposite valley Chern numbers.

We map out the valley Chern number phase diagram in the continuum model for different values of α . We see that, at small α , which corresponds to weak interlayer hopping, the Chern number is zero whenever the two masses have opposite signs. This is to be expected due to the cancellation of the Berry phase between the two layers. As we approach the strong-coupling regime (large α) the zero Chern number region shrinks in the phase diagram, and the system is mostly in the valley Chern insulator phase (see Fig. 2).

III. STUDYING COMMENSURATE LATTICES IN REAL SPACE

A. Geometry

In a lattice model or indeed a real sample of graphene, the individual valley charges are not conserved. Only the total charge is conserved and hence states in different valleys can mix. However, there is no physical difference between commensurate and incommensurate lattice models at small angles. Lattice models, whether commensurate or not, manifest the emergent symmetries of the continuum model [20] better and better as the twist angle decreases. Our reason for studying tight-binding commensurate models is twofold: We can systematically study how the bulk valley mixing effects vanish as the twist angle decreases. More importantly, the translation symmetry inherent in commensurate lattice models enables us to study wide ribbons, essential for examining the presence or absence of edge states.

We first review the geometry of commensurate TBG which is constructed from two layers of honeycomb lattices that are aligned on top of each other (AA stacking) then rotated with a relative angle θ and a possible translation between the layers. The system is not periodic for a general twist angle θ .

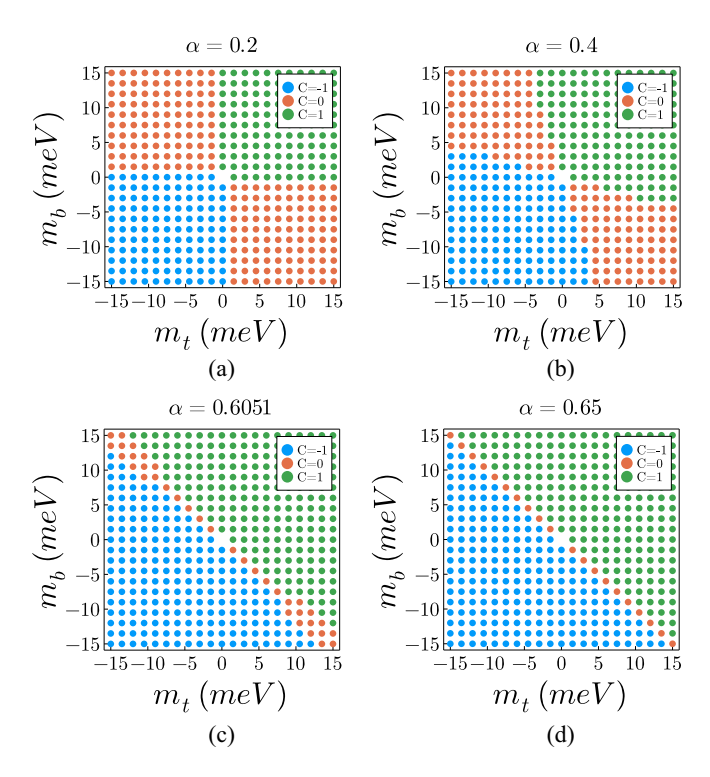


FIG. 2. Phase diagram of the valley Chern insulator phase in the continuum model. The Chern number is calculated for the conduction band near charge neutrality. (a),(b) At small interlayer coupling (small α), the quadrants with the sublattice masses on top and bottom layer (m_t, m_b) having opposite signs are in a trivial phase with zero Chern number. (c),(d) As the interlayer coupling increases, the strong renormalization of the bands leads to shrinkage of the trivial phase and to an enhancement of the valley Chern insulator. We obtained these figures using $\kappa = 0.7$ and we get a qualitatively similar phase diagram in the chiral limit ($\kappa = 0$).

However, for a set of discrete twist angles, the system has exact translation symmetry with an enlarged supercell [12,39,40] (see Fig. 3). This set of discrete twist angles is defined by co-prime positive integers (m, n) that are given by the formula

$$\cos \theta = \frac{m^2 + n^2 + 4mn}{2(m^2 + n^2 + mn)}.$$
 (4)

We assume that the top sheet rotates by angle $\theta/2$ and the bottom sheet by $-\theta/2$, the translation vectors for the superlattice are given by [41]

$$\mathbf{A}_1 = n\mathbf{a}_1^t + m\mathbf{a}_2^t, \mathbf{A}_2 = -m\mathbf{a}_1^t + (m+n)\mathbf{a}_2^t,$$
 (5)

where $\mathbf{a}_1^t = R(\theta/2)\mathbf{a}_1$ and $\mathbf{a}_2^t = R(\theta/2)\mathbf{a}_2$ are the translation vectors of the top graphene layer with $R(\theta/2)$ being the two-dimensional (2D) matrix of rotation and \mathbf{a}_1 and \mathbf{a}_2 are the unrotated graphene lattice translation vectors. The length of the supercell lattice translation vectors is expressed in terms of the rotation angle as

$$A \equiv |\mathbf{A}_1| = |\mathbf{A}_2| = \frac{(m-n)a}{2\sin\theta/2},\tag{6}$$

where a is the length of the graphene lattice constant and it is assumed that m > n. We note that, when m - n = 1, the

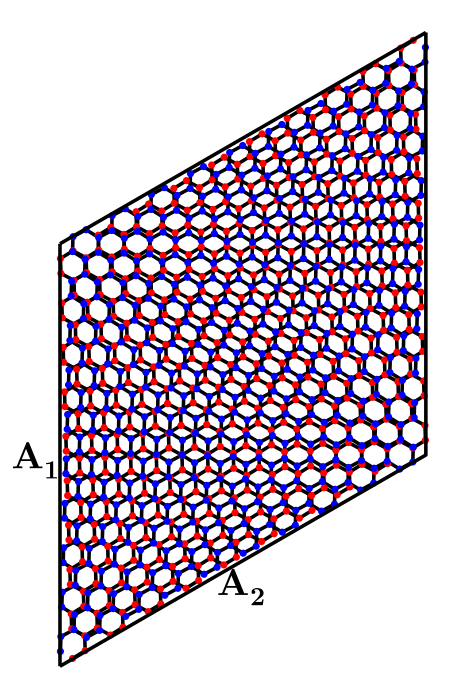


FIG. 3. An example moiré unit cell of TBG with a commensurate angle $\theta \approx 3.48^{\circ}$ ($m=10,\ n=9$) with 1084 atoms in the unit cell. ${\bf A_1}$ and ${\bf A_2}$ are the moiré lattice translation vectors. A ribbon with a generic edge can be constructed by taking ${\bf A_2}$ to be infinite and a number of moiré unit cells in the ${\bf A_1}$ direction defines the width of the ribbon.

length of the commensurate superlattice vector coincides with that of the emergent moiré pattern in the continuum. One can see that the moiré pattern grows inversely with the angle θ and, for a given m, n, the number of atoms in the unit cell (N) is given by $N = 4(m^2 + mn + n^2)$.

We conclude this section by considering the rotational symmetry of the lattice. We start with the two layers in perfect registry. In general, the center of rotation can be any point in space. However, we restrict ourselves to either rotating about a carbon site or about the center of a hexagon. Rotating about these special points leads to the system either having C_6 symmetry when rotating about the center of a hexagon [20,39,42] or a C_3 symmetry when the center of rotation is a carbon site. These symmetries are removed upon translating one of the layers in a generic direction after applying the twist.

B. Tight-binding model

We now study TBG in real space via a tight-binding model based on the carbon p_z orbital tight-binding models first introduced in graphene and then further generalized to graphene heterostructures in previous studies [41,43–45]. The Hamiltonian is given by

$$H = \sum_{\mu=1,2} \sum_{i,j} t_{ij} c_{\mu,i}^{\dagger} c_{\mu,j} + \sum_{i,j} t_{ij}^{\perp} c_{1,i}^{\dagger} c_{2,j} + \text{H.c.}, \quad (7)$$

where $c_{\mu,i}$ is annihilation operator for an electron in layer μ and at lattice position i. The first term accounts for the hopping within each graphene layer where we use the numerical value of t = -2.7 eV for the nearest-neighbor intralayer hopping strength, and set the further neighbor intralayer hoppings to

zero. The second term accounts for the interlayer hopping. To make a straightforward correspondence between the continuum and lattice models, we assume a simple form for the interlayer hopping that is a function of the in-plane distance between the two atoms (in different layers) and decays exponentially with increasing distance. The form assumed for the interlayer hopping t_{ij}^{\perp} is $t^{\perp}(r) = t_v \exp(-r/\xi)$, where r is the in-plane distance between the two atoms with ξ being the decay constant and t_v the hopping amplitude. To match the lattice calculations with the continuum model, we recall the continuum model is a function of $\alpha = w_1/(v_F k_\theta)$, and for the form of interlayer hopping chosen, w_1 is given by

$$w_1 = \frac{2\pi\xi^2}{\Omega_{u.c} (1 + k_D^2 \xi^2)^{3/2}} t_v$$

(see Appendix A for the derivation). For a given α and ξ we solve for the value of t_v that enters in the tight-binding model. The lattice relaxation effects are incorporated in the same way as in the continuum model, by reducing the AA hopping strength compared with the AB hopping strength. Finally, the HBN substrate is modeled by adding a sublattice mass term on each layer to our tight-binding Hamiltonian (7). A comparison between the band structures of the lattice model and the continuum theory has been carried out previously [41,46–48] but is provided in Appendix A for completeness. We thus have a controlled correspondence between the continuum model and the commensurately twisted lattice model. For this work, a central feature of the band structure in the commensurate supercell structure is that there is no strict separation between the valleys at finite twist angle as there was in the continuum model. Indeed the bands from both valleys of the continuum model can mix and appear superposed in the moiré Brillouin zone. However, the U(1) valley symmetry becomes better and better as the twist angle decreases. This leads to a smaller and smaller gap at the topological phase transition of the continuum model, as we will see shortly. Thus, whenever we refer to the valley Chern number, we are implicitly referring to the continuum model.

In the continuum model there is a sharp topological transition between the trivial and valley Chern insulator phases, which takes place simultaneously but independently in each valley (in the presence of time-reversal symmetry). Since this transition is accompanied by a change in the Chern number in the continuum model, a gap closing must occur in the spectrum (specifically at the K and K' points [32]). We now consider how the band structure evolves in the commensurate system as the corresponding continuum approximation is taken from a phase with zero valley Chern number to a one with nonzero valley Chern number (see Fig. 2). In addition to the U(1) valley symmetry that the continuum model has which makes the valley Chern insulator phase well defined, the continuum model also has an emergent C_3 symmetry. However, an exact C_3 symmetry is only present on the lattice when the center of rotation is a center of a hexagon or a carbon site but is removed upon carrying out a subsequent generic translation. Computing the gap between the flat bands in the tight-binding model when exact C_3 symmetry is absent, we find a tiny gap. We have checked that this gap decreases as the twist angle decreases, consistent with the valley U(1)

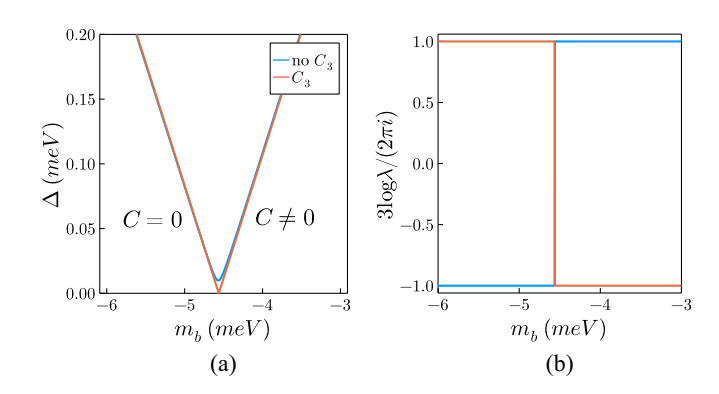


FIG. 4. The gap between the flat bands in the lattice tight-binding model. Panel (a) shows the evolution of the gap between the middle bands as we vary the Hamiltonian parameters (m_t, m_b) going through the topological transition defined by the continuum model. The path is set by $m_t = 10$ meV and varying m_b from -6 to -3 meV. A gap only closes when C_3 symmetry is present on the lattice. When an exact C_3 symmetry is absent the gap does not close and hence the trivial and valley Chern insulator phases of the continuum are smoothly connected on the lattice. (b) When C_3 symmetry is present, the two bands touching at the K point exchange their C_3 eigenvalues across the topological transition. The two figures were obtained using $\theta \approx 1.08$ (m = 31, n = 30), $\alpha = 0.6051$, $\kappa = 0.7$, and $\xi = 0.3a$. The graphene lattice constant a is set to 1.

symmetry being emergent in the lattice model at small angles. In contrast, when exact C_3 symmetry is present on the lattice, we find an exact gap closing, at the parameters corresponding to the continuum topological transition [see Fig. 4(a)], which occurs at the K or K' point. Furthermore, when C_3 symmetry is present, bands can be labeled by the C_3 eigenvalues (which we denote by λ) where λ can take any value of the cubic roots of unity $(1, \omega, \omega^2)$. The two bands that touch at the transition point exchange their C_3 eigenvalues [see Fig. 4(b)]. In the absence of C_3 symmetry (achieved in our simulation by rotating and then carrying out a generic translation) we find that the gap does not close and the two phases are connected to each other smoothly [see Fig. 4(a)].

IV. EDGE STATES IN A RIBBON GEOMETRY

A. Twisted bilayer graphene

We now turn to the motivating question of our study: Whether the moiré system when in a regime that has a valley Chern insulator in the continuum has edge states when studied in a lattice system with a boundary. Our tight-binding model allows us to get the band structure in a ribbon geometry, thus allowing access to the edge states of the TBG aligned with HBN system. An infinite ribbon can be constructed by taking the system to be infinite along one of the lattice primitive lattice vectors (A2, with momentum being a good quantum number along this direction) and finite in the other direction with the width of the ribbon set by the number of unit cells along the finite direction. Since the number of atoms in the unit cell in the ribbon geometry at small angles is quite large (the number of atoms in one moiré unit cell is $\approx 10\,000$ atoms), we only obtain the bands near charge neutrality where the most interesting physics occurs.

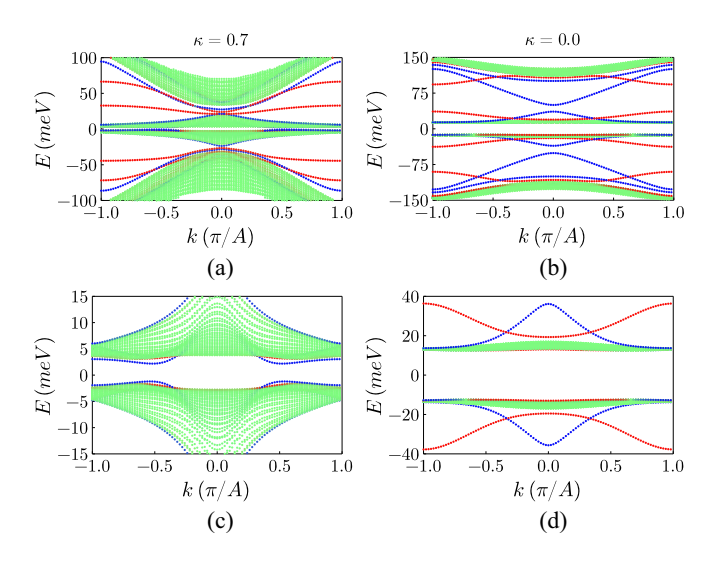


FIG. 5. Band structure of a TBG ribbon with a width of 20 moiré unit cells. We used m = 31 and n = 30 which corresponds to a commensurate angle $\theta \approx 1.08^{\circ}$ and further a generic translation between the layers is applied. The value of $\xi = 0.3$ is used. The color of the energy levels are assigned based on the average transverse location of the states—the green states are delocalized and the red and blue states are localized on the top and bottom edge respectively. Panels (b) and (d) were obtained at the chiral limit where panels (a) and (c) were obtained with $\kappa = 0.7$. The lower panels are detailed views of the upper panels in the region of energies corresponding to charge neutrality. Both layers have sublattice masses of magnitude $m_t = 15 \text{ meV}$ and $m_b = 10 \text{ meV}$, which puts the system in the valley Chern insulator phase in the continuum model. (c), (d) Absence of a dispersing gap crossing edge modes at charge neutrality is shown as we zoom in on the bands.

Upon diagonalizing this Hamiltonian, we obtain two kinds of states; those that are inherited from the infinite system (bulk bands) and states that are localized at the edge (edge states). We determine the character of the states by computing the position expectation value of the wave function along the width of the ribbon [49]. We then give each state a color that labels its character, with green denoting bulk states, and red (blue) denoting states localized on the top (bottom) edge.

We now discuss our findings for the ribbon's band structure in the chiral and the nonchiral limits. Our results for the ribbon band structure are shown in Fig. 5. We have studied the spectrum both for $\kappa = 0$ [Figs. 5(b) and 5(d)], the chiral limit and the more generic value of $\kappa = 0.7$ [Figs. 5(a) and 5(c)]. The lower panels are zoom-ins of the upper panels to emphasize the behavior close to charge neutrality. First, we find edges states, blue and red states that occur between the flat bulk bands and the higher energy bulk bands. We identify these as the "moiré edge states" which were previously studied in the literature [45,49–53]. Since these do not occur between the flat bands they will not affect the low-energy behavior at the edge at charge neutrality, which is the focus of this study. Most strikingly for our study, even when the system has mass parameters that lie in the valley Chern insulator phase within the continuum model, we find a clear absence of dispersing edge states that connect the two flat bands that acquire a nonzero Chern number in the continuum model.

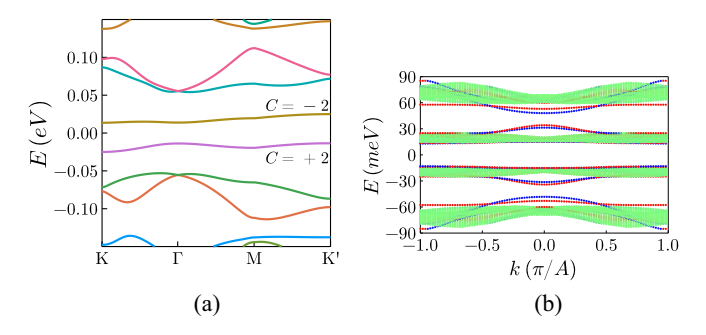


FIG. 6. Continuum model and tight-binding calculation in TDBG. Panel (a) shows the continuum model band structure obtained at $\theta = 1.3^{\circ}$ and V = 0.05 eV. The two bands in the middle have nonzero Chern number which is twice that of TBG bands. Panel (b) shows the band structure of a ribbon of width 20 moiré unit cells using the same parameters used in the continuum model and at a commensurate angle $\theta \approx 1.3^{\circ}$ (m = 26, n = 25), $\kappa = 0$, and $\xi = 0.3$. Like TBG, we do not find gap crossing edge states near charge neutrality.

We note that we have obtained the same result with different values of m_t and m_b and for different types of edges. We recall that in a naive interpretation of the continuum model, a valley Chern insulator should have valley polarized edge states with each valley contributing state of opposite chirality. Our finding appears in contradiction to this expectation. We identify two reasons for this absence. First, intervalley scattering is generically present at the edge, and, second, C_3 symmetry (whose importance was established in the previous section) is generally broken at the edge. Either effect is enough to gap out the would-be edge states associated with the valley Chern insulator in TBG.

B. Twisted double bilayer graphene

In this section we carry out a similar tight-binding calculation for the TDBG system which was the subject of the experimental study in Ref. [14] (see Fig. 6). A continuum model [12,13,54-56] can be formulated to study the bands of TDBG in the same way as for TBG. The single-valley TDBG Hamiltonian obtained by twisting two bilayers of AB stacked graphene is given by

$$H(\mathbf{r}) = \begin{pmatrix} H_{AB}^t & \tilde{U}(\mathbf{r}) \\ \tilde{U}^{\dagger}(\mathbf{r}) & H_{AB}^b \end{pmatrix}, \tag{8}$$

where the continuum model of the AB stacked graphene of the top and bottom bilayer $(H_{AB}^t$ and $H_{AB}^b)$ is given by

$$H_{AB}^{t} = \begin{pmatrix} -iv_{F}\boldsymbol{\sigma} \cdot \boldsymbol{\nabla}_{\theta/2} + \frac{V}{2} & T_{AB} \\ T_{AB}^{\dagger} & -iv_{F}\boldsymbol{\sigma} \cdot \boldsymbol{\nabla}_{\theta/2} + \frac{V}{6} \end{pmatrix}, \quad (9)$$

$$H_{AB}^{t} = \begin{pmatrix} -iv_{F}\boldsymbol{\sigma} \cdot \nabla_{\theta/2} + \frac{V}{2} & T_{AB} \\ T_{AB}^{\dagger} & -iv_{F}\boldsymbol{\sigma} \cdot \nabla_{\theta/2} + \frac{V}{6} \end{pmatrix}, \quad (9)$$

$$H_{AB}^{b} = \begin{pmatrix} -iv_{F}\boldsymbol{\sigma} \cdot \nabla_{-\theta/2} - \frac{V}{6} & T_{AB} \\ T_{AB}^{\dagger} & -iv_{F}\boldsymbol{\sigma} \cdot \nabla_{-\theta/2} - \frac{V}{2} \end{pmatrix}. \quad (10)$$

An applied electric field perpendicular to the system results into a voltage difference between the bilayers [V in Eqs. (9) and (10)]. The interlayer hopping within an AB stacked bilayer is captured in

$$T_{AB} = \begin{pmatrix} 0 & 0 \\ \gamma & 0 \end{pmatrix}, \tag{11}$$

where we only keep the direct hopping between the two layers with γ being the strength of the hopping. We use the numerical value of $\gamma = 0.361 \text{ eV}$ when we compute the band structure [57,58].

The moiré hopping between the bilayers is given by

$$\tilde{U}(\mathbf{r}) = \begin{pmatrix} 0 & 0 \\ U(\mathbf{r}) & 0 \end{pmatrix},\tag{12}$$

with $U(\mathbf{r})$ defined in equation (2). Similar to TBG, The TDBG system also has a magic angle where the two bands near charge neutrality become (almost) flat. Upon applying an electric field perpendicular to the sample, these bands get gapped and can acquire a nonzero valley Chern number with a rich phase diagram that depends on both the twist angle and the applied electric field [59]. We will focus on the case where the valence and the conduction bands have Chern numbers $C=\pm 2$. Time-reversal symmetry forces the bands in the opposite valley to have opposite Chern number so at charge neutrality the system is in the valley Chern insulator phase, as in TBG.

The lattice setup is the following; we start with two bilayers of AB stacked graphene directly on top of each other then we apply a relative twist θ between them. A semi-infinite ribbon is formed by taking the system to be infinite in one primitive superlattice direction (taken to be A_2) and finite in the other. The resulting band structure of TDBG in a ribbon geometry shows qualitatively similar behavior to TBG where there lie edge states between the flat and the high-energy bands. There are, however, no edge states that connect the two flat bands that would be associated with the valley Chern insulator phase.

V. SUMMARY AND CONCLUSIONS

We have studied the continuum model for TBG aligned with HBN substrate and the TDBG system in a perpendicular electric field where single valley bands can acquire a nonzero Chern number in both systems. Due to the presence of time-reversal symmetry, opposite valleys have opposite Chern numbers making such systems candidates for realizing a valley Chern insulator with counterpropagating valley-polarized edge modes. We then studied the problem within a tightbinding model constructed on a lattice with the two layers rotated with respect to each other by a commensurate angle where Bloch theorem is applicable. We found that C_3 symmetry in the bulk does distinguish between the zero and the nonzero Chern number bands in the continuum as seen by a gap closing at the K and K' points in the moiré BZ that occurs at the transition point between the two phases. Moreover, the two touching bands exchange their C_3 eigenvalues at the critical point. There may be further interesting physics in this fine-tuned case connected to the recently described "shift insulator" [60] that we leave for future work. We then solve the problem on a ribbon geometry where we can study the edge states of the system. Although edge states could be found

between the flat bands and higher energy bands, edge states connecting the two flat bands at charge neutrality are absent. We attribute this to the mixing of the two valleys at the edge, and to the fact that generic edges will break the C_3 symmetry of the bulk.

Our findings serve to intensify the puzzle posed by the experimental result of Ref. [14]. The experiment reports the observation of nonlocal transport, attributed to edge modes at charge neutrality in TDBG under the same conditions where we do not find edge modes. The physics missing from our model is that of electron-electron interactions. It is possible that the physical (sharp) edge is screened and modified by interactions in such a way as to reduce intervalley scattering. An extension of our model, with the addition of Coulomb interactions even at the mean-field level, can serve to investigate this possibility, which we leave for a future work.

ACKNOWLEDGMENTS

The authors are grateful to A. Vishanwath and E. Khalaf for helpful discussions. This work was supported in part by NSF DMR-2026947 (AK, RKK). G.M. is grateful to the US-Israel BSF for partial support under Grant No. 2016130. G.M. and R.K.K. acknowledge the Aspen Center for Physics, NSF PHY-1607611 (G.M., R.K.K.) for its hospitality. The authors are grateful to the University of Kentucky Center for Computational Sciences and Information Technology Services Research Computing for their support and use of the Lipscomb Compute Cluster and associated research computing resources.

APPENDIX A: COMPARISON BETWEEN THE CONTINUUM AND THE LATTICE MODEL

In this Appendix we show a comparison between the band structure obtained by our tight-binding model at a commensurate angle and the continuum models of TBG and TDBG. This also serves as a way to verify our method. First we review the derivation of the interlayer hopping in the continuum model of TBG. One starts with Bloch waves in the two layers and then compute the Hamiltonian matrix element between the two Bloch states. The resulting matrix element takes the form

$$T_{\mathbf{k}_{t}\mathbf{k}_{b}}^{\alpha\beta} = \sum_{\mathbf{G}_{t}\mathbf{G}_{b}} \tilde{t}(\mathbf{k}_{t} + \mathbf{G}_{t})e^{-i(\mathbf{k}_{t} + \mathbf{G}_{t})\cdot(\mathbf{d}_{\alpha}^{t} - \mathbf{d}_{\beta}^{b})}\delta_{\mathbf{k}_{t} + \mathbf{G}_{t}, \mathbf{k}_{b} + \mathbf{G}_{b}}, \quad (A1)$$

where \mathbf{k}_t , \mathbf{k}_b are the momenta in the top and bottom layer, respectively, and α , β are labeling the graphene sublattices with \mathbf{d}_{α}^t , \mathbf{d}_{β}^b denoting the position of the atoms within the unit cell. The sum is over the reciprocal lattice vectors $(\mathbf{G}_t, \mathbf{G}_b)$ of the top and the bottom layer. $\tilde{t}(\mathbf{k}_t + \mathbf{G}_t)$ is the Fourier transform of the interlayer hopping function and the Kronecker delta ensures the conservation of momentum. One of the main assumptions of the continuum model is restricting the sum in (A1) to the Dirac points in the graphene BZ. This rests on the fact that the hopping between the layers decays very rapidly with momentum [13,61]. Taking the form of the interlayer hopping given in the main text we have

$$\tilde{t}(q) = \int d^2 r e^{-r/\xi} e^{-i\mathbf{q}\cdot\mathbf{r}} = \frac{2\pi\xi^2}{(1+q^2\xi^2)^{3/2}},$$
 (A2)

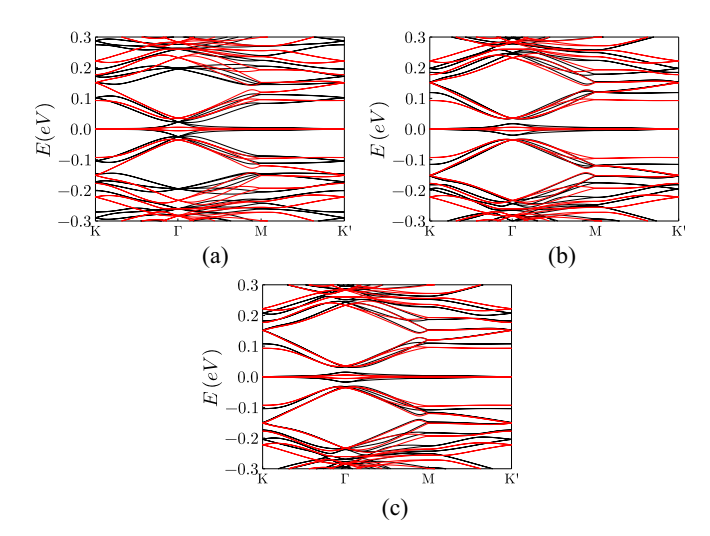


FIG. 7. Comparing the band structure obtained by the continuum and the lattice model in TBG. Both the twist angle and α are fixed at $\theta \approx 1.08^{\circ}$ (m = 31, n = 30) and $\alpha = 0.6051$. $\kappa = 0.7$ was used. The tight-binding model bands (black) are computed for different ξ going from $\xi = 0.1$ in panel (a), $\xi = 0.3$ in panel (b), and $\xi = 0.6$ in panel (c). The lattice model bands are converging to the continuum model (in red) as ξ is increasing.

which shows $\tilde{t}(q)$ is indeed a rapidly decaying function with momentum. The first-order term that enters into the continuum model is $w_1 = \tilde{t}(k_D)/\Omega_{u.c}$. The next-order hopping process beyond the Dirac points has the momentum $q = 2k_D$ with $k_D = 4\pi/3$ is the momentum of the Dirac points in the graphene BZ (the lattice constant of graphene is set to 1). The ratio between the two amplitudes is given by

$$\frac{\tilde{t}(2k_D)}{\tilde{t}(k_D)} = \left(\frac{1 + \xi^2 k_D^2}{1 + 4\xi^2 k_D^2}\right)^{3/2}.$$
 (A3)

This shows that $\tilde{t}(2k_D)$ is always less than $\tilde{t}(k_D)$ and the ratio gets smaller as ξ (the range of hopping in real space) gets bigger. There is a subtlety here, however, as one cannot keep increasing the range of the hopping uncontrollably as the continuum model is a low-energy theory which assumes the linear dispersion of the bands. Having the range of the hopping too large will send the lattice theory beyond the low-energy regime assumed in the continuum. With these restrictions in mind, we do a comparison between the band structure obtained via the lattice and the continuum model in both of TBG and TDBG. We show the bands of the lattice model converge to the continuum model bands as the range of the hopping increases (see Figs. 7 and 8).

APPENDIX B: FINITE-SIZE SCALING

In this Appendix we support our numerical findings by examining how the ribbon band structure in TBG and TDBG evolves as the width of the ribbon increases. This way we gain confidence that what we find at finite width is going to survive in the thermodynamic limit. We obtain the band structure for ribbons with successive increase in their width. We start from 5 to 10 and then reach 20 moiré unit cells. We indeed see that the bands near charge neutrality remain virtually unchanged

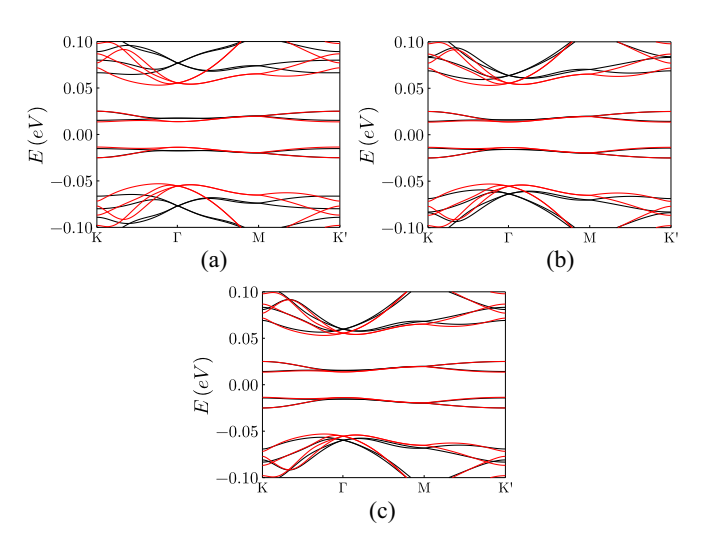


FIG. 8. Comparing the band structure obtained by the continuum and the lattice model in TDBG. Both the twist angle and α are fixed at $\theta \approx 1.3^{\circ}$ (m=26, n=25) and $\alpha=0.586$. The values of $\kappa=0.0$ and V=50 meV were used. The tight-binding model bands (black) are computed for different ξ going from $\xi=0.1$ in panel (a), $\xi=0.3$ in panel (b), and $\xi=0.6$ in panel (c). The lattice model bands are converging to the continuum model (in red) as ξ is increasing.

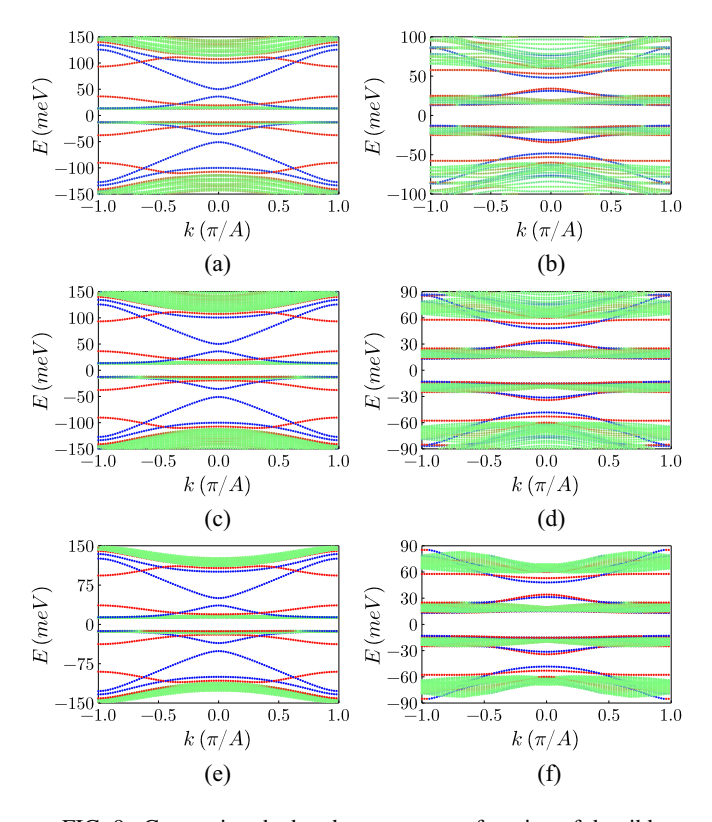


FIG. 9. Comparing the band structure as a function of the ribbon width. Panels (a), (c), (e) show the bands near charge neutrality in TBG obtained at a width of 5, 10, and 20 moiré unit cells, respectively. Panels (b), (d), (f) show the bands near charge neutrality in TDBG obtained at a width of 5, 10, and 20 moiré unit cells, respectively. In both systems we see that the bands do not change as the width is increased implying a convergence to the thermodynamic limit.

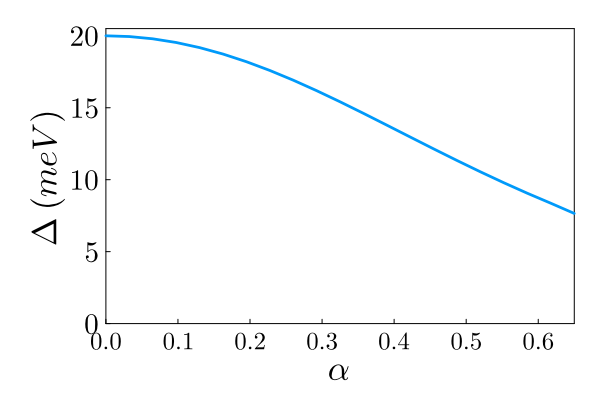


FIG. 10. Tracing the gap between the flat bands as a function of α in the continuum model. The hard gap between the two flat bands is computed as the interlayer coupling strength given by the value of α (as defined in the main text) is varying. The data are shown for the two layers have the masses $m_t = m_b = 10$ meV. The fact that gap remain open means that no Chern number has been exchanged between the valence and the conduction bands from which we can conclude that the remote bands carry zero Chern number.

(see Fig. 9) as the width of the ribbon is increased for both TBG and TDBG. The bands were obtained with $\kappa = 0.0$ for simplicity.

APPENDIX C: DO THE REMOTE BANDS CARRY CHERN NUMBER?

In this Appendix we answer the following question: Is computing the Chern number of the occupied flat band in a given valley enough to determine whether the system is a valley Chern insulator? The confounding factor is that the occupied remote bands (all bands other than the flat bands) may also carry nonzero Chern number. If the Chern number

carried by the remote occupied bands cancels that carried by the occupied flat band, the system would be trivial insulator.

We show, in a range of parameters for which the flat bands carry a nontrivial Chern number, that the occupied remote bands are trivial. Thus, in this range of parameters, computing the Chern number of the flat bands is enough to determine whether the system is a valley Chern insulator.

We approach the question indirectly. Let us take two uncoupled graphene layers, twisted with respect to each other, which gives two massive Dirac cones (from the sublattice masses m_t , m_b) as the starting point. Each massive Dirac cone from the top or bottom layer gives a contribution of $\frac{1}{2}$ sgn $(m_{t/b})$ to the Chern number. We can see that if the two masses have the same sign they add up to ± 1 Chern number for all the occupied bands together (with all the unoccupied bands together having the opposite Chern number). As the tunnel-coupling α between the layers is turned on the bands reconstruct and we reach the point where two flat bands get separated from the remote bands. Consider a point in the m_t , m_b parameter space where the occupied carry a + 1 Chern number (this occurs when m_t , m_b have the same sign). As seen in Fig. 10, the gap between the flat bands at charge neutrality remains open as α increases all the way to the value appropriate to the magic angle. This means that the sum of the Chern numbers of all occupied bands remains constant during the α evolution. Computing the Chern number of the occupied flat band at the magic angle, we get a Chern number of +1. This means that the remote bands in this case must carry zero Chern number.

The case when m_t , m_b have opposite signs is more subtle because a given point in that region can be trivial at small α but topological at large α . We are unable to make a definitive statement about the Chern number carried by the remote bands when $m_t/m_b < 0$.

- [1] Y. Cao, V. Fatemi, S. Fang, K. Watanabe, T. Taniguchi, E. Kaxiras, and P. Jarillo-Herrero, Unconventional superconductivity in magic-angle graphene superlattices, Nature (London) 556, 43 (2018).
- [2] Y. Cao, V. Fatemi, A. Demir, S. Fang, S. L. Tomarken, J. Y. Luo, J. D. Sanchez-Yamagishi, K. Watanabe, T. Taniguchi, E. Kaxiras, R. C. Ashoori, and P. Jarillo-Herrero, Correlated insulator behaviour at half-filling in magic-angle graphene superlattices, Nature (London) 556, 80 (2018).
- [3] M. Yankowitz, S. Chen, H. Polshyn, Y. Zhang, K. Watanabe, T. Taniguchi, D. Graf, A. F. Young, and C. R. Dean, Tuning superconductivity in twisted bilayer graphene, Science 363, 1059 (2019).
- [4] C. Shen, Y. Chu, Q. Wu, N. Li, S. Wang, Y. Zhao, J. Tang, J. Liu, J. Tian, K. Watanabe, T. Taniguchi, R. Yang, Z. Y. Meng, D. Shi, O. V. Yazyev, and G. Zhang, Correlated states in twisted double bilayer graphene, Nat. Phys. 16, 520 (2020).
- [5] X. Liu, Z. Hao, E. Khalaf, J. Y. Lee, Y. Ronen, H. Yoo, D. Haei Najafabadi, K. Watanabe, T. Taniguchi, A. Vishwanath, and P. Kim, Tunable spin-polarized correlated states in twisted double bilayer graphene, Nature (London) 583, 221 (2020).

- [6] Y. Cao, D. Rodan-Legrain, O. Rubies-Bigorda, J. M. Park, K. Watanabe, T. Taniguchi, and P. Jarillo-Herrero, Tunable correlated states and spin-polarized phases in twisted bilayer–bilayer graphene, Nature (London) 583, 215 (2020).
- [7] G. W. Burg, J. Zhu, T. Taniguchi, K. Watanabe, A. H. MacDonald, and E. Tutuc, Correlated Insulating States in Twisted Double Bilayer Graphene, Phys. Rev. Lett. 123, 197702 (2019).
- [8] M. He, Y. Li, J. Cai, Y. Liu, K. Watanabe, T. Taniguchi, X. Xu, and M. Yankowitz, Symmetry breaking in twisted double bilayer graphene, Nat. Phys. 17, 26 (2021).
- [9] G. Chen, L. Jiang, S. Wu, B. Lyu, H. Li, B. L. Chittari, K. Watanabe, T. Taniguchi, Z. Shi, J. Jung, Y. Zhang, and F. Wang, Evidence of a gate-tunable Mott insulator in a trilayer graphene moiré superlattice, Nat. Phys. 15, 237 (2019).
- [10] G. Chen, A. L. Sharpe, P. Gallagher, I. T. Rosen, E. J. Fox, L. Jiang, B. Lyu, H. Li, K. Watanabe, T. Taniguchi, J. Jung, Z. Shi, D. Goldhaber-Gordon, Y. Zhang, and F. Wang, Signatures of tunable superconductivity in a trilayer graphene moiré superlattice, Nature (London) 572, 215 (2019).
- [11] G. Chen, A. L. Sharpe, E. J. Fox, Y.-H. Zhang, S. Wang, L. Jiang, B. Lyu, H. Li, K. Watanabe, T. Taniguchi, Z. Shi,

- T. Senthil, D. Goldhaber-Gordon, Y. Zhang, and F. Wang, Tunable correlated Chern insulator and ferromagnetism in a moiré superlattice, Nature (London) **579**, 56 (2020).
- [12] J. M. B. Lopes dos Santos, N. M. R. Peres, and A. H. Castro Neto, Graphene Bilayer with a Twist: Electronic Structure, Phys. Rev. Lett. 99, 256802 (2007).
- [13] R. Bistritzer and A. H. MacDonald, Moiré bands in twisted double-layer graphene, Proc. Natl. Acad. Sci. USA 108, 12233 (2011).
- [14] Y. Wang, J. Herzog-Arbeitman, G. W. Burg, J. Zhu, K. Watanabe, T. Taniguchi, A. H. MacDonald, B. A. Bernevig, and E. Tutuc, Bulk and edge properties of twisted double bilayer graphene, Nat. Phys. 18, 48 (2022).
- [15] N. N. T. Nam and M. Koshino, Lattice relaxation and energy band modulation in twisted bilayer graphene, Phys. Rev. B 96, 075311 (2017).
- [16] P. Lucignano, D. Alfè, V. Cataudella, D. Ninno, and G. Cantele, Crucial role of atomic corrugation on the flat bands and energy gaps of twisted bilayer graphene at the magic angle $\theta \sim 1.08^{\circ}$, Phys. Rev. B **99**, 195419 (2019).
- [17] G. Tarnopolsky, A. J. Kruchkov, and A. Vishwanath, Origin of Magic Angles in Twisted Bilayer Graphene, Phys. Rev. Lett. 122, 106405 (2019).
- [18] E. Suárez Morell, J. D. Correa, P. Vargas, M. Pacheco, and Z. Barticevic, Flat bands in slightly twisted bilayer graphene: Tight-binding calculations, Phys. Rev. B 82, 121407(R) (2010).
- [19] H. C. Po, L. Zou, A. Vishwanath, and T. Senthil, Origin of Mott Insulating Behavior and Superconductivity in Twisted Bilayer Graphene, Phys. Rev. X 8, 031089 (2018).
- [20] L. Zou, H. C. Po, A. Vishwanath, and T. Senthil, Band structure of twisted bilayer graphene: Emergent symmetries, commensurate approximants, and Wannier obstructions, Phys. Rev. B 98, 085435 (2018).
- [21] J. Kang and O. Vafek, Symmetry, Maximally Localized Wannier States, and a Low-Energy Model for Twisted Bilayer Graphene Narrow Bands, Phys. Rev. X 8, 031088 (2018)
- [22] J. Jung, A. M. DaSilva, A. H. MacDonald, and S. Adam, Origin of band gaps in graphene on hexagonal boron nitride, Nat. Commun. 6, 6308 (2015).
- [23] J. Jung, E. Laksono, A. M. DaSilva, A. H. MacDonald, M. Mucha-Kruczyński, and S. Adam, Moiré band model and band gaps of graphene on hexagonal boron nitride, Phys. Rev. B 96, 085442 (2017).
- [24] B. Hunt, J. D. Sanchez-Yamagishi, A. F. Young, M. Yankowitz, B. J. LeRoy, K. Watanabe, T. Taniguchi, P. Moon, M. Koshino, P. Jarillo-Herrero, and R. C. Ashoori, Massive Dirac fermions and Hofstadter butterfly in a van der Waals heterostructure, Science 340, 1427 (2013).
- [25] F. Amet, J. R. Williams, K. Watanabe, T. Taniguchi, and D. Goldhaber-Gordon, Insulating Behavior at the Neutrality Point in Single-Layer Graphene, Phys. Rev. Lett. 110, 216601 (2013).
- [26] A. A. Zibrov, E. M. Spanton, H. Zhou, C. Kometter, T. Taniguchi, K. Watanabe, and A. F. Young, Even-denominator fractional quantum Hall states at an isospin transition in monolayer graphene, Nat. Phys. 14, 930 (2018).
- [27] H. Kim, N. Leconte, B. L. Chittari, K. Watanabe, T. Taniguchi, A. H. MacDonald, J. Jung, and S. Jung, Accurate gap determination in monolayer and bilayer graphene/h-BN moiré superlattices, Nano Lett. 18, 7732 (2018).

- [28] D. Wong, Y. Wang, J. Jung, S. Pezzini, A. M. DaSilva, H.-Z. Tsai, H. S. Jung, R. Khajeh, Y. Kim, J. Lee, S. Kahn, S. Tollabimazraehno, H. Rasool, K. Watanabe, T. Taniguchi, A. Zettl, S. Adam, A. H. MacDonald, and M. F. Crommie, Local spectroscopy of moiré-induced electronic structure in gate-tunable twisted bilayer graphene, Phys. Rev. B 92, 155409 (2015).
- [29] M. Serlin, C. L. Tschirhart, H. Polshyn, Y. Zhang, J. Zhu, K. Watanabe, T. Taniguchi, L. Balents, and A. F. Young, Intrinsic quantized anomalous Hall effect in a moiré heterostructure, Science 367, 900 (2020).
- [30] A. L. Sharpe, E. J. Fox, A. W. Barnard, J. Finney, K. Watanabe, T. Taniguchi, M. A. Kastner, and D. Goldhaber-Gordon, Emergent ferromagnetism near three-quarters filling in twisted bilayer graphene, Science 365, 605 (2019).
- [31] X. Lu, P. Stepanov, W. Yang, M. Xie, M. A. Aamir, I. Das, C. Urgell, K. Watanabe, T. Taniguchi, G. Zhang, A. Bachtold, A. H. MacDonald, and D. K. Efetov, Superconductors, orbital magnets and correlated states in magic-angle bilayer graphene, Nature (London) 574, 653 (2019).
- [32] N. Bultinck, S. Chatterjee, and M. P. Zaletel, Mechanism for Anomalous Hall Ferromagnetism in Twisted Bilayer Graphene, Phys. Rev. Lett. 124, 166601 (2020).
- [33] Y.-H. Zhang, D. Mao, Y. Cao, P. Jarillo-Herrero, and T. Senthil, Nearly flat Chern bands in moiré superlattices, Phys. Rev. B 99, 075127 (2019).
- [34] Y.-H. Zhang, D. Mao, and T. Senthil, Twisted bilayer graphene aligned with hexagonal boron nitride: Anomalous Hall effect and a lattice model, Phys. Rev. Res. 1, 033126 (2019).
- [35] N. Bultinck, E. Khalaf, S. Liu, S. Chatterjee, A. Vishwanath, and M. P. Zaletel, Ground State and Hidden Symmetry of Magic-Angle Graphene at Even Integer Filling, Phys. Rev. X 10, 031034 (2020).
- [36] J. Liu, Z. Ma, J. Gao, and X. Dai, Quantum Valley Hall Effect, Orbital Magnetism, and Anomalous Hall Effect in Twisted Multilayer Graphene Systems, Phys. Rev. X 9, 031021 (2019).
- [37] Y. Su and S.-Z. Lin, Current-Induced Reversal of Anomalous Hall Conductance in Twisted Bilayer Graphene, Phys. Rev. Lett. 125, 226401 (2020).
- [38] F. Wu and S. Das Sarma, Collective Excitations of Quantum Anomalous Hall Ferromagnets in Twisted Bilayer Graphene, Phys. Rev. Lett. 124, 046403 (2020).
- [39] E. J. Mele, Commensuration and interlayer coherence in twisted bilayer graphene, Phys. Rev. B **81**, 161405(R) (2010).
- [40] S. Shallcross, S. Sharma, E. Kandelaki, and O. A. Pankratov, Electronic structure of turbostratic graphene, Phys. Rev. B 81, 165105 (2010).
- [41] P. Moon and M. Koshino, Optical absorption in twisted bilayer graphene, Phys. Rev. B **87**, 205404 (2013).
- [42] Z. Song, Z. Wang, W. Shi, G. Li, C. Fang, and B. A. Bernevig, All Magic Angles in Twisted Bilayer Graphene are Topological, Phys. Rev. Lett. 123, 036401 (2019).
- [43] G. Trambly de Laissardière, D. Mayou, and L. Magaud, Localization of Dirac electrons in rotated graphene bilayers, Nano Lett. **10**, 804 (2010).
- [44] J. C. Slater and G. F. Koster, Simplified LCAO method for the periodic potential problem, Phys. Rev. **94**, 1498 (1954).
- [45] W. Landgraf, S. Shallcross, K. Türschmann, D. Weckbecker, and O. Pankratov, Electronic structure of twisted graphene flakes, Phys. Rev. B 87, 075433 (2013).

- [46] F. Guinea and N. R. Walet, Continuum models for twisted bilayer graphene: Effect of lattice deformation and hopping parameters, Phys. Rev. B 99, 205134 (2019).
- [47] M. Koshino and N. N. T. Nam, Effective continuum model for relaxed twisted bilayer graphene and moiré electron-phonon interaction, Phys. Rev. B 101, 195425 (2020).
- [48] Y. Su and S.-Z. Lin, Pairing symmetry and spontaneous vortexantivortex lattice in superconducting twisted-bilayer graphene: Bogoliubov-de Gennes approach, Phys. Rev. B 98, 195101 (2018).
- [49] M. Fujimoto and M. Koshino, Moiré edge states in twisted bilayer graphene and their topological relation to quantum pumping, Phys. Rev. B **103**, 155410 (2021).
- [50] E. Suárez Morell, R. Vergara, M. Pacheco, L. Brey, and L. Chico, Electronic properties of twisted bilayer nanoribbons, Phys. Rev. B 89, 205405 (2014).
- [51] E. S. Morell, P. Vargas, P. Häberle, S. A. Hevia, and L. Chico, Edge states of moiré structures in graphite, Phys. Rev. B 91, 035441 (2015).
- [52] J. Liu, J. Liu, and X. Dai, Pseudo Landau level representation of twisted bilayer graphene: Band topology and implications on the correlated insulating phase, Phys. Rev. B **99**, 155415 (2019).
- [53] M. Fleischmann, R. Gupta, D. Weckbecker, W. Landgraf, O. Pankratov, V. Meded, and S. Shallcross, Moiré edge states

- in twisted graphene nanoribbons, Phys. Rev. B **97**, 205128 (2018).
- [54] N. R. Chebrolu, B. L. Chittari, and J. Jung, Flat bands in twisted double bilayer graphene, Phys. Rev. B 99, 235417 (2019).
- [55] Y. W. Choi and H. J. Choi, Intrinsic band gap and electrically tunable flat bands in twisted double bilayer graphene, Phys. Rev. B 100, 201402(R) (2019).
- [56] M. Koshino, Band structure and topological properties of twisted double bilayer graphene, Phys. Rev. B 99, 235406 (2019).
- [57] J. Jung and A. H. MacDonald, Accurate tight-binding models for the π bands of bilayer graphene, Phys. Rev. B **89**, 035405 (2014).
- [58] A. H. Castro Neto, F. Guinea, N. M. R. Peres, K. S. Novoselov, and A. K. Geim, The electronic properties of graphene, Rev. Mod. Phys. 81, 109 (2009).
- [59] Y.-X. Wang, F. Li, and Z.-Y. Zhang, Phase diagram and orbital Chern insulator in twisted double bilayer graphene, Phys. Rev. B 103, 115201 (2021).
- [60] S. Liu, A. Vishwanath, and E. Khalaf, Shift Insulators: Rotation-Protected Two-Dimensional Topological Crystalline Insulators, Phys. Rev. X 9, 031003 (2019).
- [61] R. Bistritzer and A. H. MacDonald, Transport between twisted graphene layers, Phys. Rev. B **81**, 245412 (2010).